Atomic Fe on hierarchically ordered porous carbon towards high-performance Lithium-sulfur batteries

Atomic Fe on hierarchically ordered porous carbon towards High-performance Lithium-sulfur batteries

Xinan Chen[a], Zhengju Zhu[a,*], Elif Vargun[c], Yiwen Li[a], Petr Saha[b], Qilin Cheng[a,b,*]

[a]*Key Laboratory for Ultrafine Materials of Ministry of Education, Shanghai Engineering Research Center of Hierarchical Nanomaterials, School of Materials Science and Engineering, East China University of Science and Technology, 200237 Shanghai, China*

[b]*Sino-EU Joint Laboratory of New Energy Materials and Devices, Tomas Bata University in Zlin, nam. T. G. Masaryka 5555, 760 01 Zlin, Czech Republic*

[c]*Department of Chemistry, Mugla Sitki Kocman University, 48000 Mugla, Turkey*

[*]*Corresponding authors at: Key Laboratory for Ultrafine Materials of Ministry of Education, Shanghai Engineering Research Center of Hierarchical Nanomaterials, School of Materials Science and Engineering, East China University of Science and Technology, 200237 Shanghai, China (Z. Zhu, Q. Cheng).*

ABSTRACT

Lithium-sulfur (Li-S) battery is the promising next-generation energy storage device owing to its ultra-high theoretical energy density and low cost. Unfortunately, its practical performance is significantly hindered by the poor conductivity of sulfur, huge volume change, and soluble lithium polysulfides ($LiPSs$). To address above issues, single iron (Fe) atoms anchored on hierarchically porous carbon substrate configured by ordered macropores and widespread mesopores/micropores (Fe—N—C/OC) are synthesized and acted as carbon hosts for sulfur cathodes. Single Fe atoms in Fe-N_4 moieties serve as active sites to accelerate conversion kinetics of $LiPSs$ due to strong catalytic ability, thereby the shuttle effect being obviously restrained. Meanwhile, the trimodal-porous structure provides continuous carbon framework for enhanced electrical conductivity, ordered macroporous channels bridged by mesopores for rapid Li^+ diffusion, and adequate spaces to reserve sulfur volume oscillation. Consequently, sulfur-loaded Fe—N—C/OC (Fe—N—C/OC/S) cathodes exhibit an impressive specific capacity of 1442 mAh g^{-1} at 0.1C and maintain the capacity retention of 89.2 % after 300 cycles at 1C. It offers fresh insights for designing efficient sulfur hosts to enhance the performance of Li-S batteries.

Keywords: Lithium-sulfur batteries, single atom catalyst, polysulfide conversion, hierarchically porous carbon, electrochemistry

1. Introduction

The fast development of transportable electronic devices, electric vehicles, and smart grids accelerates the requirement for energy storage devices with high energy density and low cost [**1**]. Due to the excellent theoretical specific capacity and ultra-high energy density, lithium-sulfur ($Li-S$) batteries

are considered as promising candidates for next-generation battery systems [**2**,**3**]. Meanwhile, sulfur is environmentally friendly, cost-effective, and earth-abundant, conducive to mass production and manufacture [**4-7**]. Despite the above-mentioned merits, the application and development of $Li-S$ batteries are hindered by some drawbacks derived from the multielectron and multiphase reaction mechanism [**8**]. Specifically, the large volume change occurs during the charge-discharge process, and the poor conductivity of sulfur and its discharged products retards the electron transfer, resulting in sluggish reaction kinetics [**9-11**]. More importantly, the intermediate lithium polysulfide ($LiPS$) could dissolve into organic electrolyte and undergo the migration between sulfur cathodes and lithium anodes, chemically and electrochemically participating in both electrodes. This phenomenon, namely, the shuttle effect, could lead to the degradation of Li anodes, low sulfur utilization, and the permanent capacity fading [**12-14**].

To address the issues on the conductivity and volume change of sulfur cathode, conductive microporous/mesoporous carbon is employed as sulfur hosts to increase the contact areas with insulating sulfur/ lithium sulfide ($Li2S$), resulting in shortened electron transport distance, and accommodate the sulfur volume change in the electrochemical reaction [**15-17**]. With assistance of microporous/mesoporous carbon, the poor conductivity of sulfur has been reliably alleviated with sufficient pore space for sulfur reservoir. But it is worth noting that the full and partial fill with sulfur could cause kinetic inhibition to ion diffusion within carbons. Notably, carbon materials with hierarchically porous structure, including abundant micropores/mesopores to immobilize sulfur and interconnected macropores to provide a free pathway for electron/ion transportation, could construct a collaborative sulfur host to boost overall performance of $Li-S$ batteries [**18**,**19**]. On the other hand, carbon materials have limited capability to restrain the shuttle effect of immediate LiPSs or to promote the redox reactions between soluble $LiPSs$ and solid $Li2S$ because of the nonpolar nature of carbons hard to adsorb polar $LiPSs$ [**15**].

To further suppress the shuttle effect, various polar species, such as metal oxides [**20**,**21**], nitrides [**22**,**23**], and sulfides [**24**,**25**] have been incorporated into porous carbon to improve the affinity of $LiPSs$. Nevertheless, these metal-based inorganics are generally nanoparticles and large aggregates in different morphology and therefore normally give rise to depressed surface area, conductivity and pore volume of carbon hosts, further causing the low sulfur utilization and blocking of pore channels for electron/ion. Compared with metal-based inorganics, single atoms with monodisperse transition-metal centers possess a theoretical 100 % utilization efficiency, unsaturated metal species, and special electronic structure [**26-28**]. As a result, single atoms anchored on carbon substrates as electrocatalytic active sites not only immobilize LiPSs through the binding ability of central metal atoms and S_n^{2-} in $LiPS$, but also expedite the kinetics of sulfur redox reactions [**29-31**]. To this end, the controllable anchoring of metal atoms on hierarchically porous carbon with well-developed micropores/meso-pores and interconnected macropores could integrate respective merits to solve drawbacks of $Li-S$ battery.

In this work, single Fe atoms are successfully anchored on a microsized trimodal-porous carbon substrates integrating micropores, meso-pores, and ordered macropores (Fe—N—C/OC) as a cathode for $Li-S$ batteries. Zeolite imidazole framework ($ZIF-8$) is employed as carbon sources with polystyrene spheres (PS) as sacrificial templates to form hierarchically porous structure. Fe ions are introduced into ZIF-8 by a chemical doping approach and transformed to Fe-N4 coordination structure during the pyrolysis. The trimodal-porous carbon performs significant functions in a sulfur-infiltrated Fe—N—C/OC (Fe—N—C/ OC/S) cathode. It is important to have bridging mesopores in between macropores to construct a continuous three-dimensional ($3D$) carbon network to ensure good electrical conductivity, sufficient space for sulfur volume oscillation, easy access to the electron/ion,

and large exposure of atomic Fe to $LiPS$. Since Fe—N—C/OC with Fe-N_4 structures includes active single Fe atoms, it is able to accelerate sulfur redox reactions via the highly catalytic activity. This work demonstrates a feasible strategy for designing functional cathodes with enhanced catalytic properties in $Li-S$ batteries.

2. Experimental section

2.1. Preparation of single Fe atoms on hierarchically ordered porous carbon (Fe—N—C/OC)

Polystyrene sphere (PS) (diameter of 300 nm) was synthesized firstly according to the reported work [**32**]. The styrene monomer without stabilizer was injected into a round bottom flask, mixed with 0.25 L of water and 0.5 g of PVP, and then bubbled using N_2 for 15 min. After that, above solution was stirred under N_2 atmosphere at 75 °C for 20 min, and then 0.1 g $K_2S_2O_8$ was added as initiator. The synthetic reaction lasted 24 h with stirring under nitrogen atmosphere. The monodisperse PS emulsion was obtained and corresponding PS ordered templates were obtained by the vacuum filtration.

$Zn(NO_3)_2{\cdot}6H_2O$ (8.15 g), $Fe(NO_3)_3{\cdot}9H_2O$ (100 mg) and 2-methylimidazole (6.75 g) were added in 45 mL methanol. Then, ordered PS template was immersed in the above mixture for 1 h and degassed for 15 min in the vacuum. After that, the impregnated PS template was filtrated and dried at 50 °C for several hours, then was further transferred to a mixed solution of 45 mL methanol and ammonia solution (Vmethanol: Vammonia = 2: 1) and degassed again in the vacuum for 15 min to ensure the homogeneous permeation of the solvent into the template. After soaking for 24 h, Fe doped $ZIF-8$ embedded inside the PS monolith (Fe-ZIF-8@PS) was formed, and then filtered and dried in air. The Fe-ZIF-8@PS was heated to 1000 °C at the rate of 5 °C/min under N_2 flow and kept at this temperature for 2 h to obtain Fe—N—C/OC.

For comparison, N-doped ordered macroporous carbon (N—C/OC) was prepared via the analogous method of Fe—N—C/OC but without adding of 100 mg $Fe(NO_3)_3{\cdot}9H_2O$. Single Fe atoms on carbon (Fe—N—C) and N-doped carbon (N—C) were also synthesized as control samples according to the previous report [**33**].

2.2. Preparation of different sulfur cathodes

0.1 g as-prepared Fe—N—C/OC and 0.3 g sulfur were ground into the fine powder, and then the mixture was transferred into an Ar-protected Teflon container in 155 °C oven for 24 h. After that, Fe—N—C/ OC/S composite was collected. The synthesis of Fe—N—C/S, N—C/ OC/S, and N—C/S composites were similar to that of Fe—N—C/OC/S.

2.3. Material characterization

The crystal structure, morphologies and microstructures of all the samples were measured by X-ray diffraction (XRD, Rigaku D/max 2550VB/PC), field emission scanning electron microscopy (FESEM, Hitachi S4800), transmission electron microscopy (TEM, JEOL JEM-2100), and scanning transmission electron microscopy (STEM, ThermoFisher Talos F200X), respectively. N_2 adsorption-desorption isotherms were carried out on a Brunauer-Emmett-Teller (BET) surface area analyzer (Micromeritics ASAP 2460). Element composition was investigated by X-ray photoelectron spectroscopy (XPS, ESCALAB 250Xi). Raman scattering was performed using a Laser Micro-Raman Spectrometer (Renishaw

inVia Reflex). Fe K-edge X-ray absorption fine structure spectra were collected at the wiggler XAS Beamline (12ID) at the Australian Synchrotron in Melbourne. Data treatment and analysis were processed with the Athena software.

2.4. Assembly of symmetric batteries

Symmetric CR2016 coin cells were assembled with 0.5 M Li2S6 electrolyte (40 pL), a Celgard 2400 separator, and two identical active electrodes (Fe—N—C/OC or N—C/OC, the active material loading is $\sim$ 1.0 mg cm^{-2}). To evaluate polysulfide redox conversion kinetics, all the CV measurement was performed between — 0.8 and 0.8 V with a scan rate of 20 mV s^{-1}.

2.5. Li_2S nucleation

The active electrodes (Fe—N—C/OC or N—C/OC) and lithium foils were utilized as cathode and anode to assemble CR2032 coin cells, while 0.5 M Li_2S_8 electrolyte (20 μL) and traditional electrolyte without Li_2S_8 (20 μL) were chosen as catholyte and anolyte, respectively. For Li_2S nucleation, the cells were performed by discharging to 2.06 V at 0.112 mA, followed by discharging potentiostatically at 2.05 V until the current dropped below 10 —5 A.

2.6. Electrochemical measurements

Cathode slurry was prepared by mixing 70 wt% Fe—N—C/OC/S (N—C/OC/S or Fe—N—C/S or N—C/S) composite, 20 wt% Super P and 10 wt% polyvinylidene fluoride (PVDF) in the N-methyl pyrroli-done (NMP) solvent. The slurry was then coasted onto an aluminum foil and dried in the vacuum oven at 60 °C for 12 h. Next, the electrode film was cut into discs of 12 mm diameter and with a sulfur loading of $\sim$ 1.0 mg cm^{-2}. 2032-type coin cells were assembled utilizing as-prepared cathodes, lithium metal anodes, Celgard 2400 separator, and electrolyte in the Ar-filled glove box. The electrolyte was composed of 1.0 M lithium bis-trifluoromethanesulfonimide ($LiTFSI$) and 1 wt% $LiNO_3$ in 1,3-dioxolane and 1,2-dimethoxyethane (volume ratio = 1: 1). LAND CT2001A was employed to conduct the charge/ discharge measurements. And the CHI660E electrochemical station was chosen to perform the cyclic voltammetry (CV) in the range of 1.7 to 2.8 V and electrochemical impedance spectroscopy (EIS) from 100 kHz to 0.01 Hz with a potential amplitude of 5 mV.

3. Result and discussion

As illustrated in **Fig. 1**a, Fe—N—C/OC is fabricated by combination of chemical doping, template-induced assembly and subsequent pyrolysis process. Traditionally, pre-synthesized PS microspheres are firstly assembled into $3D$ ordered PS templates (**Fig. S1**a-b). Then, Fe-ZIF-8@PS is synthesized by introducing Fe^{3+} ions during the growth of $ZIF-8$ on PS template in the methanol/ammonia mixture (**Fig. S1**c), and further pyrolyzed at 1000 °C to remove self-sacrificed PS template below 500 °C (**Fig. S2**) and carbonize $ZIF-8$ to hierarchically porous carbons with the anchoring of Fe atoms. As indicated by **Fig. 1**b-d, SEM and TEM images of Fe—N—C/OC display a tetrakaidecahedron morphology with $3D$ ordered macropores ($\sim$200 nm), which is interconnected by mesopores with dozens of nanometers (**Fig. S3**). Besides the mesoporous channels, high-resolution TEM image also confirms the mesoporous structure with the pore size of 5-15 nm spreading the carbon layers (**Fig. S4**), indicating

the large inner surface and interconnected volume. As a contrast, N—C/OC was prepared without adding Fe^{3+} ions, which has the same morphology to Fe—N—C/OC (**Fig. S5**), indicating the introduction of Fe^{3+} ion during the growth of $ZIF-8$ would not affect the morphology. Furthermore, Fe—N—C and N—C were synthesized without employing PS templates (**Figs. S6-S7**). Obviously, these control samples have the well-defined rhombic dodecahedron shapes, different than the morphology of Fe—N—C/OC owing to the shaping effect of PS templates.

To further verify pore structure characteristics, N_2 adsorption-desorption isotherms are carried out and relative data are presented in **Table S1**. Fe—N—C/OC possesses a type IV isotherm (**Fig. 1**d), indicating the contribution from mesoporous structure [34]. In addition, the increasing adsorption capacity at the end of Fe—N—C/OC curve also verifies the existence of macroporous structure. The mesoporosity of Fe—N—C/OC could be identified with dominant mesopores ranging from 5 to 40 nm with the average size of 2.66 nm, whose pore volume reaches 0.71 $cm^3\ g^{-1}$ with 46.4 % contributed by mesopores, providing a large inner space to accommodate the sulfur species and volume expansion of sulfur. Furthermore, the specific surface area (SSA) based on BET theory of Fe—N—C/OC is 1068 m^2/g. The high SSA and macroporosity of Fe—N—C/OC provide more electrochemical active interfaces and wide ion transport channels to facilitate the redox of $LiPS$. In contrast, Fe—N—C without PS template only exhibits a type I curve with absent mesoporosity and macroporosity, whose pore volume is greatly reduced to 0.53 $cm^3\ g^{-1}$ confirming the significant function of PS template to create mesopores and macropores. Consequently, the trimodal-porous structure configured by ordered macropores interconnected through mesopores is constructed in Fe—N—C/OC, which could accommodate sulfur volume change, provide conductive surfaces, and favor fast transport of ion. Single Fe atoms on hierarchically porous carbons are further visualized regarding the distribution and the coordination environment. XPS survey spectra reveal the existence of C, N, and O elements in Fe—N—C/OC and N—C/OC. Moreover, Fe element also exists in Fe—N—C/OC (**Fig. S8**). The XRD patterns (**Fig. S9**) of Fe—N—C/OC, Fe—N—C, and N—C/OC exhibit two broad amorphous peaks at 25° and 44° respectively, indexed to (002) and (101) planes of graphitic carbon [**35**], indicating a graphitized feature. The graphitic nature of Fe—N—C/OC is also verified by the Raman spectrum (**Fig. S10**). Furthermore, it is lack of signal belonging to the Fe crystal in the XRD pattern of Fe—N—C/OC. High angle annular dark field (HAADF)-STEM is utilized to understand the Fe—N—C/OC at a subangstrom resolution. A mass of bright dots are uniformly distributed on hierarchically porous carbons (**Fig. 2**a), explicitly demonstrating single Fe atoms due to the atomic number contrast. Additionally, energy dispersive spectra (EDS) mapping reveals the uniform distribution of atomic Fe on hierarchically porous carbons (**Fig. S11**), in consistent with the HAADF-STEM image.

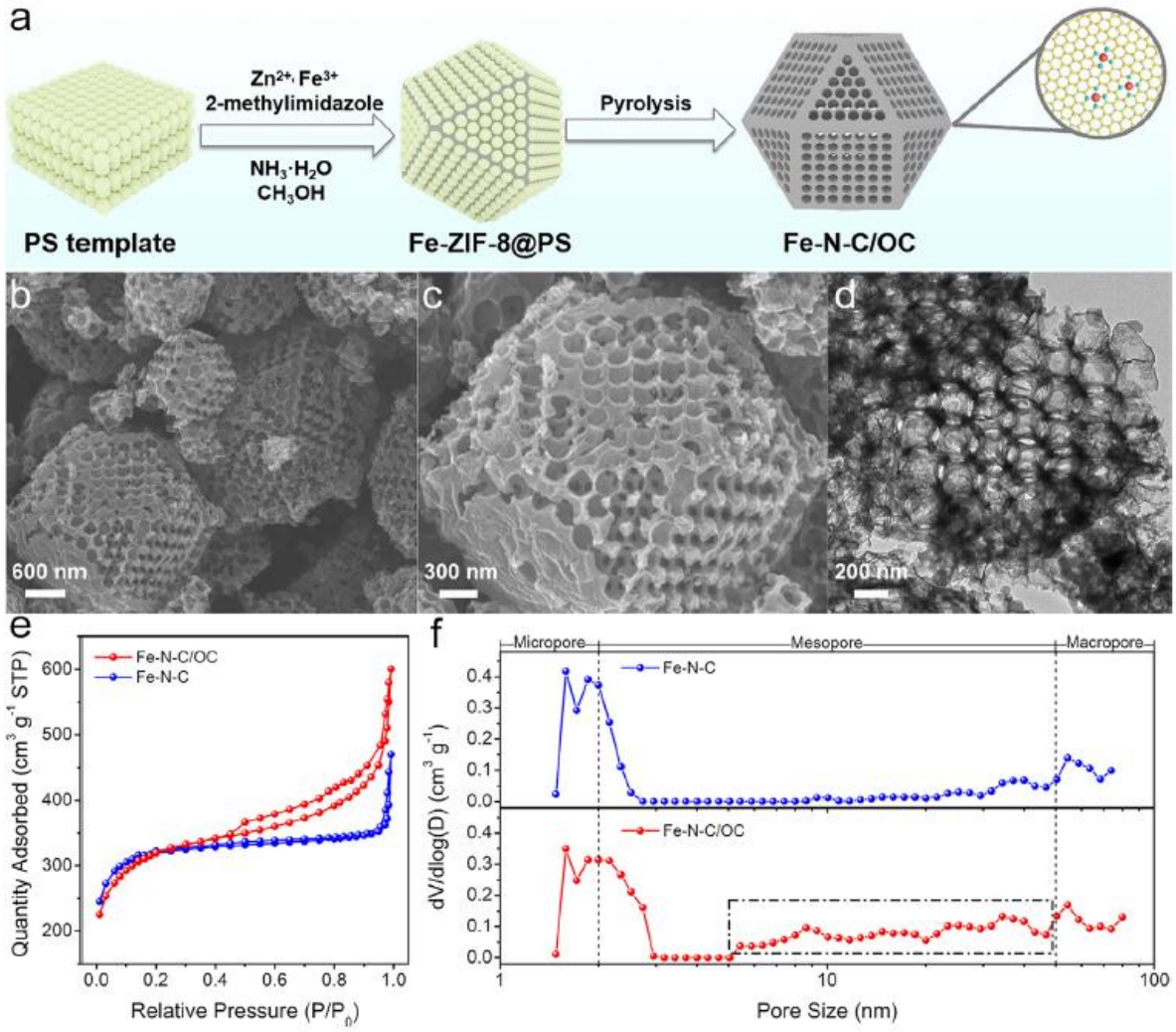

Fig. 1. (a) Schematic illustration for the synthesis of Fe—N—C/OC. (b,c) SEM and (d) TEM images of Fe—N—C/OC. (e) N_2 adsorption-desorption isotherms and (f) Pore-size distributions of Fe—N—C/OC and Fe—N—C.

The chemical environment of single Fe atoms is firstly evaluated by high-resolution N 1 s XPS spectrum (**Fig. 2**b), which reveals species including pyridinic-N at 398.5 eV, pyrrolic-N at 399.1 eV, graphitic-N at 401.0 eV, and oxidized-N at 402.6 eV, implying the presence of Fe-N_x coordination environment. To verify this hypothesis, the Fe K-edge X-ray absorption near edge structure (XANES) spectra (**Fig. 2**c) are carried out and show that pre-edge profile of Fe—N—C/OC is close to that of iron phthalocyanine (FePc), which suggests that atomic Fe is coordinated with four N atoms to form a square-planar Fe-N_4 molecular structure, in accordance with results of XPS [**36**]. In addition, similar absorption edge between Fe—N—C/OC and FePc demonstrates that the valence state of Fe in Fe—N—C/OC is $+2$. In the K-edge extended X-ray absorption fine structure ($EXAFS$) spectra (**Fig. 2**d), the main peak of Fe—N—C/OC located at 1.44 A corresponds to FeN bond, almost identical to that of FePc (1.47 A). The absence of peak around 2.23 A from EXAFS spectrum further certifies only atomic Fe instead of Fe-Fe metallic bonds. Thus, it is concluded that single Fe atoms forms Fe-N_4 moieties on hierarchically porous carbons.

To reveal the catalytic effect of single Fe atoms on polysulfide conversion reaction, symmetric cells with Fe—N—C/OC as working and counter electrodes, 0.5 M L2S6 as the electrolyte were assembled [**37**,**38**]. The Fe—N—C/OC cell exhibits the higher polarization current than that of N—C/OC cell in CV curves (**Fig. 3**a). It suggests that Fe—N—C/OC has stronger electrocatalytic effect on the kinetic

conversion of the $LiPSs$ because of the contribution of Fe-N_4 moieties. The potentiostatic nucleation experiments were also carried out to explore the electrochemical deposition from liquid $LiPSs$ to solid Li_2S. For Fe—N—C/OC-based cells, the redox peak appears earlier than that of N—C/OC-based cells with higher discharging current peak. Moreover, the Li_2S nucleation capacity of Fe—N—C/OC (236.36 mAh g^{-1}) is much higher than the Li_2S formation on the N—C/OC (145.42 mAh g^{-1}), manifesting its superiority in the nucleation and deposition of Li_2S. The higher capacity of Li_2S precipitation reveals that Fe-N_4 moieties in Fe—N—C/OC electrocatalyze the redox reactions from soluble $LiPSs$ to solid Li_2S and accelerate the Li_2S deposition on hierarchically porous carbons.

As carbonaceous supports, Fe—N—C/OC and other control samples were employed to prepare Fe—N—C/OC/S (**Fig. S12**), N—C/OC/S, Fe—N—C/S and N—C/S composites with controlled S mass (1.0 mg cm^{-2}) for further electrochemical evaluation.

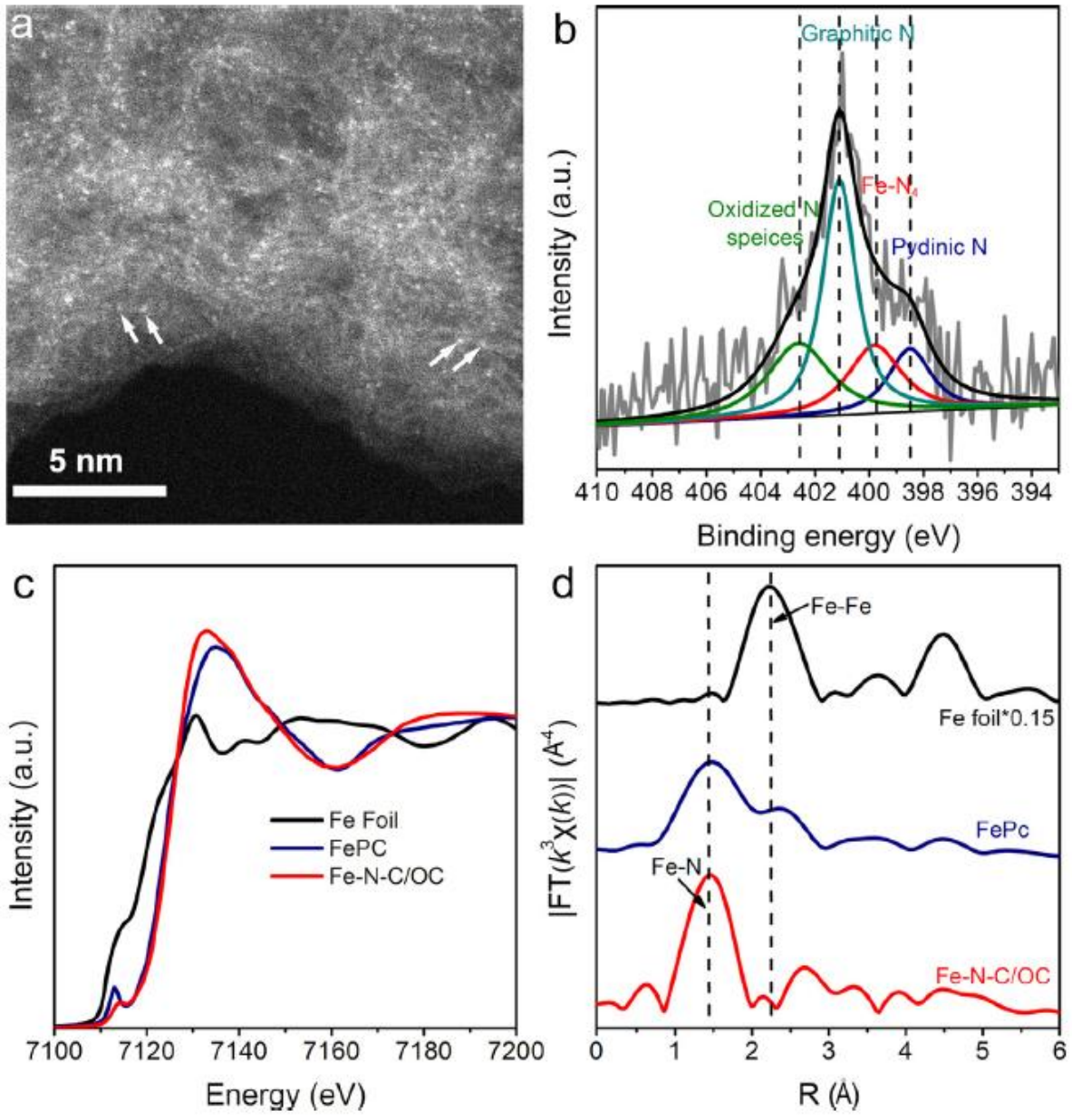

Fig. 2. (a) HAADF-STEM image and (b) N 1 s XPS spectrum of Fe—N—C/OC. (c) $XANES$ spectra and (d) Fourier transforms of EXAFS spectra at Fe K-edge of Fe—N—C/OC, Fe metal foil, and FePc.

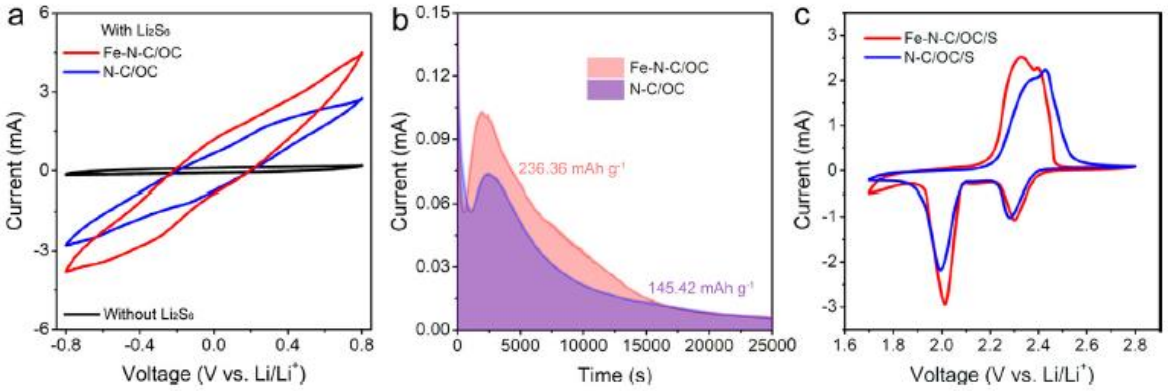

Fig. 3. (a) CV curves at a scan rate of 20 mV s 1 of symmetric cells with Fe—N—C/OC or Fe—N—C electrodes. (b) Potentiostatic nucleation curves of Li-S cells with Fe—N—C/OC or Fe—N—C cathodes. (c) CV curves of Li-S cells with Fe—N—C/OC/S or Fe—N—C/S cathodes.

$Li-S$ cells assembled by Fe—N—C/OC/S and N—C/OC/S cathodes exhibit two cathodic peaks and overlapped anodic peaks, representing the multiple reaction mechanism. Two sharp cathodic peaks at 2.32 V and 2.01 V correspond to the reaction from elemental sulfur to $LiPS$ and $LiPS$ further to Li2S2/Li2S. In contrast, overlapped anodic peaks relate to reversed reactions from lithium sulfide to LiPSs and sulfur. Fe—N—C/OC/S cathode exhibited apparently negative shift in the anodic peak and positive shift in the cathodic peak. Furthermore, the sharper and higher peak at 2.01 V demonstrates the enhanced kinetics of liquid-solid deposition, consistent with results from potentiostatic nucle-ation experiments. The sulfur kinetics is also quantitatively verified by Tafel slopes. Both Tafel slopes for redox peaks a and b decrease from NC/OC/S cathode to Fe—N—C/OC/S cathode (**Fig. S13**). These results indicate the enhanced kinetics derive from superior electrocatalytic activity of single Fe atoms.

Fig. 4a presents CV curves of Fe—N—C/OC/S cell from 1 to 3cycles at 0.1 mV s^{-1}. Impressively, well-defined reduction peaks and oxidization peaks are observed, manifesting the high stability and reversibility of sulfur-related redox reactions. The galvanostatic discharge-charge (GDC) profiles (**Fig. 4**b) show that Fe—N—C/OC/S cathodes signify the lowest polarization potential (134.2 mV) and the initial capacity of 1442 mAh g^{-1} at 0.1C (1C = 1675 mAh g^{-1}), outperforming those of Fe—N—C/S (697 mAh g^{-1}), N—C/OC/ S (860 mAh g^{-1}), and N—C/S (642 mAh g^{-1}). Moreover, it is little shift of voltage platforms for Fe—N—C/OC/S cathodes with increased current densities (**Fig. S14**). The two discharge voltage plateaus corresponding to reduction reactions were well maintained at 2C, indicative of the excellent redox kinetics of LiPSs caused by single Fe atoms and hierarchically porous structures. At higher cycling rates of 0.2, 0.5, 1, 2, and 3C, the cells equipped with Fe—N—C/OC/S cathodes deliver the discharge capacities of 1028 mAh g-1, 859 mAh g^{-1}, 800 mAh g^{-1}, 746 mAh g^{-1}, and 660 mAh g^{-1} (**Fig. 4**c), respectively, considerably higher than those of control samples. Impressively, Fe—N—C/OC/S cathode could still achieve the capacity of 846 mAh g^{-1} after 50 cycles with different current densities as switched back to 0.2C, indicating a satisfied electrochemical reversibility.

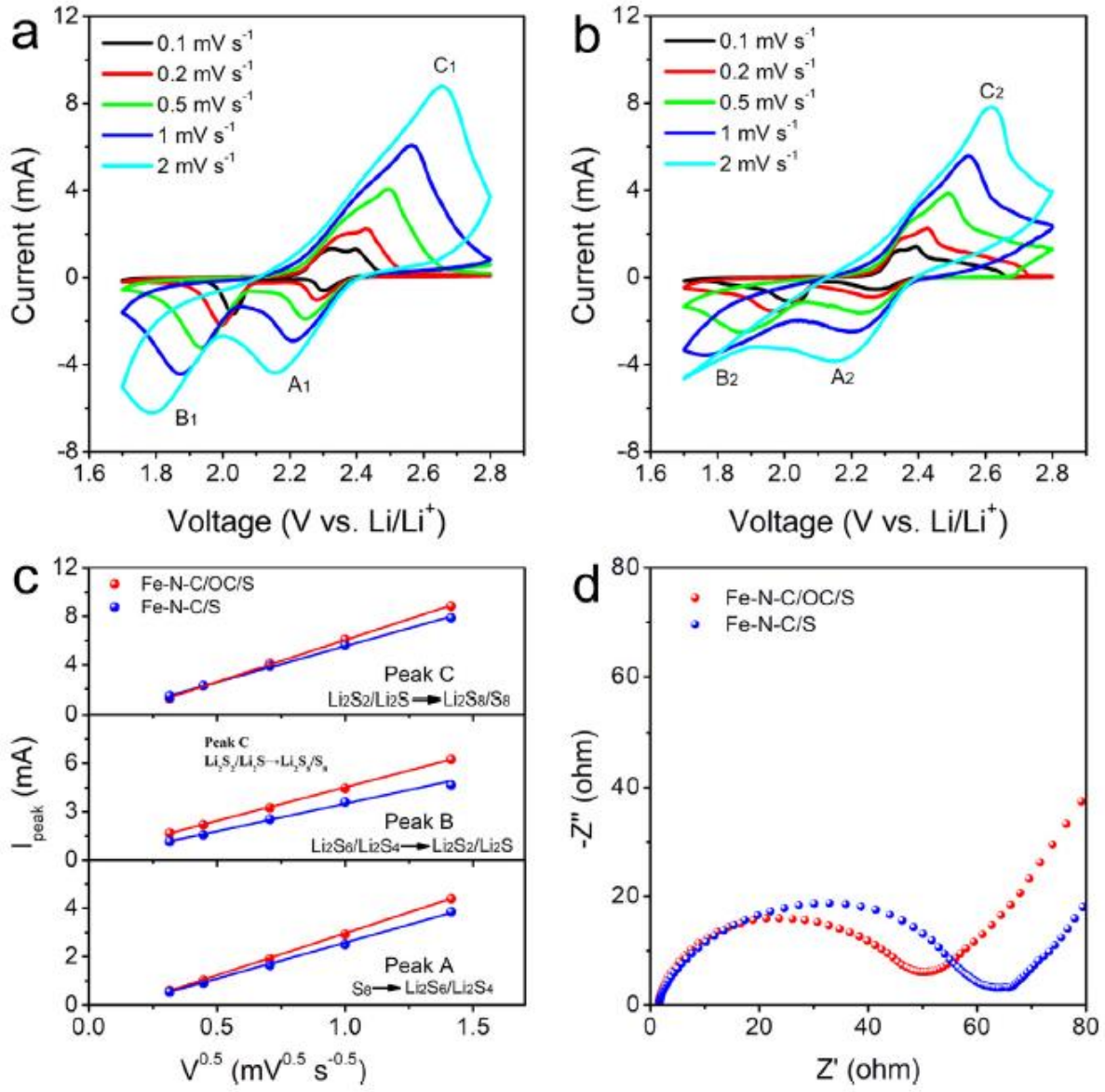

Fig. 4. (a) CV curves of $Li-S$ cells with Fe—N—C/OC/S cathodes. (b) Charge/discharge profiles at 0.1C, (c) Rate performance, and (d) Cycling performances at 1C of $Li-S$ cells with Fe—N—C/OC/S, N—C/OC/S, Fe—N—C/S, and N—C/S cathodes. (e) Cycling performances of $Li-S$ cells with Fe—N—C/OC/S cathodes with sulfur loading 2.3 and 3.1 mg cm^{-2}.

Apart from outstanding rate performances, the Fe—N—C/OC/S cathode endows the batteries with the remained capacity of 712 mAh g^{-1} after 300 cycles at 1C (**Fig. 4**d), corresponding to a capacity retention of 89.2 % (0.036 % per cycle) and the Coulombic efficiency above 97 %, which is comparable to other reported cathode materials (**Table S2**), and much lower than those of Fe—N—C/S (0.102 % per cycle), N—C/OC/S (0.098 % per cycle), and N—C/S (0.140 % per cycle). This is because that superior catalytic activity of single Fe atoms and high sulfur utilization from trimodal-porous carbon substrates. The sulfur loading is considered as another critical factor for the practical applications of $Li-S$ systems. **Fig. 4**f shows cycling performances of Fe—N—C/OC/S cathodes with higher sulfur loadings (2.3 and 3.1 mg cm^{-2}) at 1C, which contribute initial areal capacities of 1.6 and 2.0 mAh cm^{-2} (specific capacities of 712 and 639 mAh g^{-1}), respectively. After cycling for 100 cycles at 1C, the areal capacities retained 1.5 and 1.8 mAh cm^{-2} (specific capacities of 674 and 575 mAh g^{-1}), corresponding to 93.8 % and 90.0 % of the initial capacity. These results indicate highly stable S electrochemistry.

The lithium-ion diffusion performances were further characterized by CV curves recorded during 0.1 to 2.0 mV s^{-1} (**Fig. 5**a-b). The redox peak currents increase linearly with square roots of sweep rates, implying the diffusion-controlled redox process. And lithium-ion diffusion coefficence $(\mathrm{D}_{\mathrm{Li}}^{+})$ is determined through the Randles-Sevcik equation [**39**]. Notably, Fe—N—C/OC/S cathode exhibits a larger slope (**Fig. 5**c), which means that the trimodal-porous carbon substrate is conducive to promote lithium-ion diffusion during charge/discharge and expose more Fe-N_4 moieties active sites towards $LiPSs$ conversion. To further reveal the conductivity of this hierarchically porous carbons, the electrochemical impedance spectroscopy (EIS) was conducted and presented in **Fig. 5**d. Both Nyquist plots c4onsisted of depressed semicircles and inclined lines in the different frequency region (**Fig. S15**). The intercept at the real axis Z' reflects the internal resistance (R_s) from electrolyte and cell parts. The Fe—N—C/OC/S cathode possesses the smaller R_s values (1.58 Ω) by comparison with the Fe—N—C/S cathode (1.59 Ω). The diameter of the semicircle is referred to the charge transfer resistance (R_{ct}) [**40**], and Fe—N—C/ OC/S cathode had the lower R_{ct} (52 Ω) than that of the Fe—N—C/S cathode (65 Ω), verifying enhanced conductivity and the faster charge-transfer capability caused by the hierarchically porous structure.

4. Conclusion

In conclusion, single Fe atoms were successfully loaded on the hierarchically porous carbon with ordered macropores and abundant mesopores/micropores. The unique Fe-N_4 moieties could catalyze the conversion of the $LiPS$, effectively limiting the migration of the $LiPS$ and suppressing the shuttle effect. Moreover, well-defined trimodal-porous nanostructure renders the sulfur electrically conducting, promotes the transport of electron/ion to active sulfur, and accommodates volume expansion during the operation. Consequently, the $Li-S$ battery was sharply improved with assistance of Fe—N—C/OC/S cathodes, which exhibits a high initial specific capacity of 1442 mAh g^{-1} at 0.1C and a low-capacity degradation rate of 0.036 % during 300 cycles. This finding provides a compatible strategy combining porous conductive hosts with single atom catalysts to address the drawbacks of sulfur electrochemistry, inspiring the development of energy storage devices including multielectron chemistry.

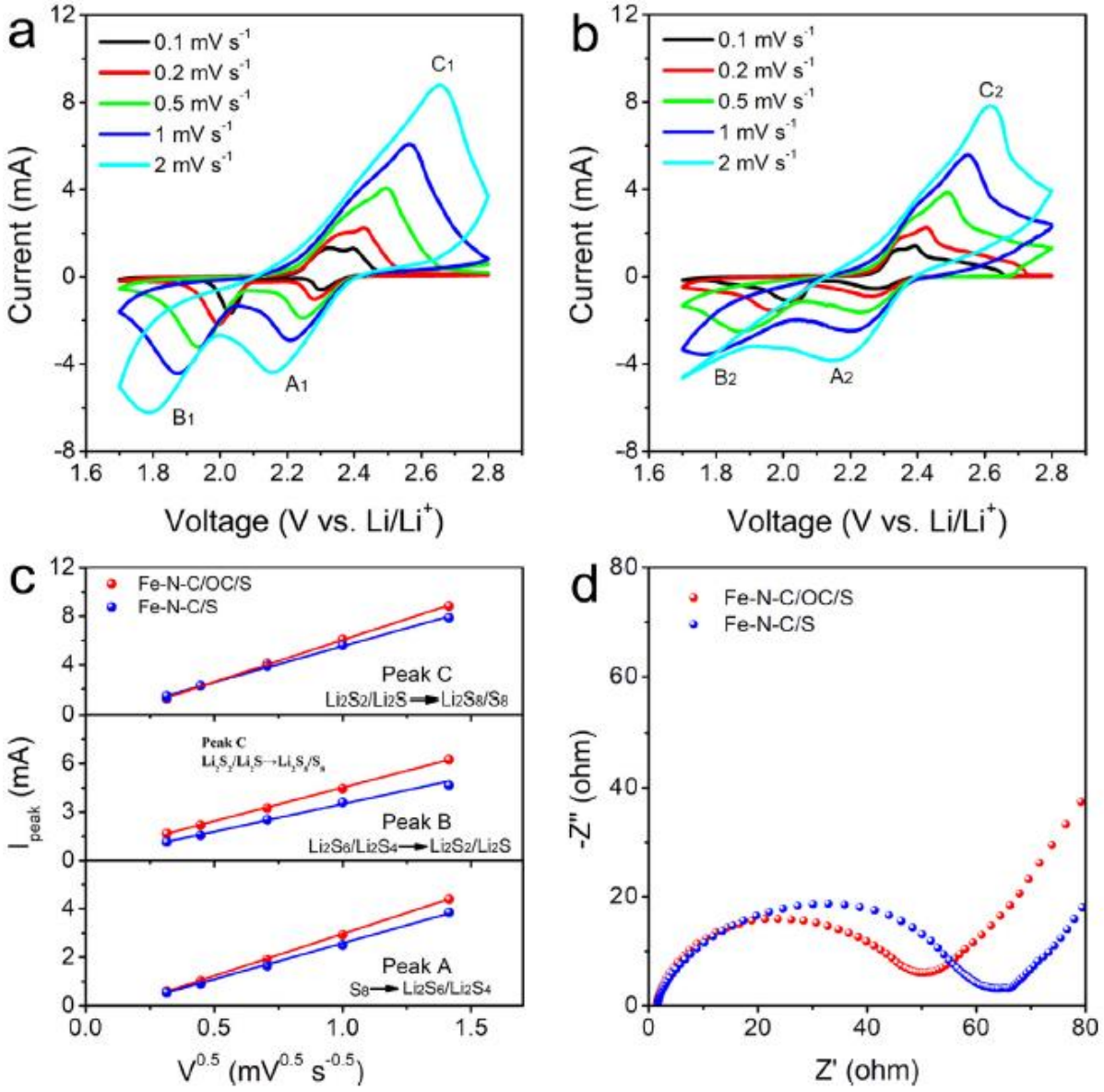

Fig. 5. CV curves from 0.1 to 2.0 mV s 1 of $Li-S$ cells with (a) Fe—N—C/OC/S cathodes (b) Fe—N—C/S cathodes. (c) The relationship between the peak currents (A, B, C) and square root of the scan rates. (d) EIS spectra of $Li-S$ cells with Fe—N—C/OC/S cathodes and Fe—N—C/S cathodes.

References

[1] C. Ma, Y.Q. Zhang, Y.M. Feng, N. Wang, L.J. Zhou, C.P. Liang, L.B. Chen, Y.Q. Lai, X.B. Ji, C.L. Yan, W.F. Wei, Engineering Fe-N coordination structures for fast redox conversion in lithium-sulfur batteries, Adv. Mater. 33 (2021) 2100171.

[2] K.L. Zhang, W.L. Cai, Y.F. Liu, G. Hu, W.W. Hu, Y.Z. Kong, X.J. Zhang, L.B. Wang, G. Li, Nitrogen-doped carbon embedded with Ag nanoparticles for bidirectionally-promoted polysulfide redox electrochemistry, Chem. Eng. J. 427 (2022) 130897.

[3] G.R. Li, S. Wang, Y.N. Zhang, M. Li, Z.W. Chen, J. Lu, Revisiting the role of polysulfides in lithium-sulfur batteries, Adv. Mater. 30 (2018) 1705590.

[4] G. Li, X.L. Wang, M.H. Seo, M. Li, L. Ma, Y.F. Yuan, T.P. Wu, A.P. Yu, S. Wang, J. Lu, Z.W. Chen, Chemisorption of polysulfides through redox reactions with organic molecules for lithium-sulfur batteries, Nat. Commun. 9 (2018) 705.

[5] T.T. Nguyen, J. Balamurugan, H.W. Go, Q.P. Ngo, N.H. Kim, J.H. Lee, Dualfunctional Co5.47N/Fe3N heterostructure interconnected 3D N-doped carbon nanotube-graphene hybrids for accelerating polysulfide conversion in Li-S batteries, Chem. Eng. J. 427 (2022) 131774.

[6] T. Yan, Y.u. Wu, F. Gong, C. Cheng, H. Yang, J. Mao, K. Dai, L. Cheng, T. Cheng, L. Zhang, TiH2 nanodots exfoliated via facile sonication as bifunctional electrocatalysts for Li-S batteries, ACS Appl. Mater. Interfaces 14 (5) (2022) 6937-6944.

[7] R.R. Chu, T.T. Nguyen, Y.Q. Bai, N.H. Kim, J.H. Lee, Uniformly controlled treble boundary using enriched adsorption sites and accelerated catalyst cathode for robust lithium-sulfur batteries, Adv. Energy Mater. 12 (2022) 2102805.

[8] A. Manthiram, Y. Fu, Y.-S. Su, Challenges and prospects of lithium-sulfur batteries, Acc. Chem. Res. 46 (5) (2013) 1125-1134.

[9] Y. Hu, W. Chen, T.Y. Lei, Y. Jiao, J.W. Huang, A.J. Hu, C.H. Gong, C.Y. Yan, X.F. Wang, J. Xiong, Strategies toward high-loading lithium-sulfur battery, Adv. Energy Mater. 10 (2020) 2000082.

[10] H.J. Peng, J.Q. Huang, X.B. Cheng, Q. Zhang, Review on high-loading and high-energy lithium-sulfur batteries, Adv. Energy Mater. 7 (2017) 1700260.

[11] D. Zhang, S. Wang, R.M. Hu, J. Gu, Y. Cui, B. Li, W.H. Chen, C.T. Liu, J.X. Shang, S. B. Yang, Catalytic conversion of polysulfides on single atom zinc implanted mxene toward high-rate lithium-sulfur batteries, Adv. Funct. Mater. 30 (2020) 2002471.

[12] H. Li, Y. Li, L. Zhang, Designing principles of advanced sulfur cathodes toward practical lithium-sulfur batteries, SusMat 2 (1) (2022) 34-64.

[13] C. Ma, Y.M. Feng, X.J. Liu, Y. Yang, L.J. Zhou, L.B. Chen, C.L. Yan, W.F. Wei, Dual-engineered separator for highly robust, all-climate lithium-sulfur batteries, Energy Storage Mater. 32 (2020) 46-54.

[14] Y.J. Liu, D.H. Hong, M.Q. Chen, Z. Su, Y.F. Gao, Y.Y. Zhang, D.H. Long, Synergistic action of Pt and Nb2O5 ultrafine nanoparticles for bidirectional conversion of polysulfides in high-performance lithium-sulfur cells, Chem. Eng. J. 430 (2022) 132714.

[15] J. Xie, B.Q. Li, H.J. Peng, Y.W. Song, M. Zhao, X. Chen, Q. Zhang, J.Q. Huang, Implanting atomic cobalt within mesoporous carbon toward highly stable lithium-sulfur batteries, Adv. Mater. 31 (2019) 1903813.

[16] J.B. Kang, X.H. Tian, C.Z. Yan, L.Y. Wei, L. Gao, J.G. Ju, Y.X. Zhao, N.P. Deng, B. Cheng, W.M. Kang, Customized structure design and functional mechanism analysis of carbon spheres for advanced lithium-sulfur batteries, Small 18 (2022) 2104469.

[17] S. Kwon, H. Song, N. ^akmakgi, Y. Jeong, A practical approach to design sulfur host material for lithium-sulfur batteries based on electrical conductivity and pore structure, Mater. Today Commun. 27 (2021) 102309.

[18] X. Ji, K.T. Lee, L.F. Nazar, A highly ordered nanostructured carbon-sulphur cathode for lithium-sulphur batteries, Nat. Mater. 8 (6) (2009) 500-506.

[19] J.B. Liu, C.C. Hu, W.J. Gao, H.P. Li, Y. Zhao, Combined enhanced redox kinetics and physiochemical confinement in three-dimensionally ordered macro/ mesoporous TiN for highly stable lithium-sulfur batteries, Nanotechnology 33 (2021) 115401.

[20] L. Ma, R. Chen, G. Zhu, Y.i. Hu, Y. Wang, T. Chen, J. Liu, Z. Jin, Cerium oxide nanocrystal embedded bimodal micromesoporous nitrogen-rich carbon nanospheres as effective sulfur host for lithium-sulfur batteries, ACS Nano 11 (7) (2017) 7274-7283.

[21] Q. Sun, B.J. Xi, J.Y. Li, H.Z. Mao, X.J. Ma, J.W. Liang, J.K. Feng, S.L. Xiong, Nitrogen-doped graphene-supported mixed transition-metal oxide porous particles to confine polysulfides for lithium-sulfur batteries, Adv. Energy Mater. 8 (2018) 1800595.

[22] Y. Fan, Z. Yang, W.X. Hua, D. Liu, T. Tao, M.M. Rahman, W.W. Lei, S.M. Huang, Y. Chen, Functionalized boron nitride nanosheets/graphene interlayer for fast and long-life lithium-sulfur batteries, Adv. Energy Mater. 7 (2017) 1602380.

[23] T. Zhou, W. Lv, J. Li, G. Zhou, Y. Zhao, S. Fan, B. Liu, B. Li, F. Kang, Q.-H. Yang, Twinborn TiO2-TiN heterostructures enabling smooth trapping-diffusion-conversion of polysulfides towards ultralong life lithium-sulfur batteries, Energy Environ. Sci. 10 (7) (2017) 1694-1703.

[24] X. Liu, J.Q. Huang, Q. Zhang, L.Q. Mai, Nanostructured metal oxides and sulfides for lithium-sulfur batteries, Adv. Mater. 29 (2017) 1601759.

[25] C. Ye, L. Zhang, C.X. Guo, D.D. Li, A. Vasileff, H.H. Wang, S.Z. Qiao, A 3D hybrid of chemically coupled nickel sulfide and hollow carbon spheres for high performance lithium-sulfur batteries, Adv. Funct. Mater. 27 (2017) 1702524.

[26] K. Zhang, Z. Chen, R. Ning, S. Xi, W. Tang, Y. Du, C. Liu, Z. Ren, X. Chi, M. Bai, C. Shen, X. Li, X. Wang, X. Zhao, K. Leng, S.J. Pennycook, H. Li, H. Xu, K.P. Loh, K. Xie, Single-atom coated separator for robust lithium-sulfur batteries, ACS Appl. Mater. Interfaces 11 (28) (2019) 25147-25154.

[27] J. Yang, Z.Y. Qiu, C.M. Zhao, W.C. Wei, W.X. Chen, Z.J. Li, Y.T. Qu, J.C. Dong, J. Luo, Z.Y. Li, Y. Wu, In situ thermal atomization to convert supported nickel nanoparticles into surface-bound nickel single-atom catalysts, Angew. Chem. Int. Ed. 57 (2018) 14095-14100.

[28] Z. Du, X. Chen, W. Hu, C. Chuang, S. Xie, A. Hu, W. Yan, X. Kong, X. Wu, H. Ji, L.-J. Wan, Cobalt in nitrogen-doped graphene as single-atom catalyst for high-sulfur content lithium-sulfur batteries, J. Am. Chem. Soc. 141 (9) (2019) 3977-3985.

[29] Y.J. Li, P. Zhou, H. Li, T.T. Gao, L. Zhou, Y.L. Zhang, N. Xiao, Z.H. Xia, L. Wang, Q. H. Zhang, L. Gu, S.J. Guo, A freestanding flexible single-atom cobalt-based multifunctional interlayer toward reversible and durable lithium-sulfur batteries, Small Methods 4 (2020) 1900701.

[30] C. Zhao, G.-L. Xu, Z. Yu, L. Zhang, I. Hwang, Y.-X. Mo, Y. Ren, L. Cheng, C.-J. Sun, Y. Ren, X. Zuo, J.-T. Li, S.-G. Sun, K. Amine, T. Zhao, A high-energy and long-cycling lithium-sulfur pouch cell via a macroporous catalytic cathode with doubleend binding sites, Nat. Nanotechnol. 16 (2) (2021) 166-173.

[31] L.L. Zhang, D.B. Liu, Z. Muhammad, F. Wan, W. Xie, Y.J. Wang, L. Song, Z.Q. Niu, J. Chen, Single nickel atoms on nitrogen-doped graphene enabling enhanced kinetics of lithium-sulfur batteries, Adv. Mater. 31 (2019) 1903955.

[32] Z.J. Zhu, H.J. Yin, Y. Wang, C.H. Chuang, L. Xing, M.Y. Dong, Y.R. Lu, G. Casillas-Garcia, Y.L. Zheng, S. Chen, Y.H. Dou, P.R. Liu, Q.L. Cheng, H.J. Zhao, Coexisting single-atomic Fe and Ni sites on hierarchically ordered porous carbon as a highly efficient ORR electrocatalyst, Adv. Mater. 32 (2020) 2004670.

[33] X. Wan, X. Liu, Y. Li, R. Yu, L. Zheng, W. Yan, H. Wang, M. Xu, J. Shui, Fe-N-C electrocatalyst with dense active sites and efficient mass transport for high-performance proton exchange membrane fuel cells, Nat. Catal. 2 (3) (2019) 259-268.

[34] S.H. Lee, J. Kim, D.Y. Chung, J.M. Yoo, H.S. Lee, M.J. Kim, B.S. Mun, S.G. Kwon, Y. E. Sung, T. Hyeon, Design principle of Fe-N-C electrocatalysts: How to optimize multimodal porous structures, J. Am. Chem. Soc. 141 (2019) 2035-2045.

[35] A.Q. Zhu, L.L. Qiao, P.F. Tan, Y.J. Ma, W.X. Zeng, R. Dong, C. Ma, J. Pan, Iron-nitrogen-carbon species for oxygen electro-reduction and Zn-air battery: Surface engineering and experimental probe into active sites, Appl. Catal. B: Environ. 254 (2019) 601-611.

[36] X. Ao, W. Zhang, Z. Li, J.-G. Li, L. Soule, X. Huang, W.-H. Chiang, H.M. Chen, C. Wang, M. Liu, X.C. Zeng, Markedly enhanced oxygen reduction activity of singleatom Fe catalysts via integration with Fe nanoclusters, ACS Nano. 13 (10) (2019) 11853-11862.

[37] H.D. Shi, X.M. Ren, J.M. Lu, C. Dong, J. Liu, Q.H. Yang, J. Chen, Z.S. Wu, Dualfunctional atomic zinc decorated hollow carbon nanoreactors for kinetically accelerated polysulfides conversion and dendrite free lithium sulfur batteries, Adv. Energy Mater. 10 (2020) 2002271.

[38] L. Luo, J. Li, H. Yaghoobnejad Asl, A. Manthiram, In-situ assembled VS4 as a polysulfide mediator for high-loading lithium-sulfur batteries, ACS Energy Lett. 5 (4) (2020) 1177-1185.

[39] H. Xia, K. Zhang, B. Luo, H. Hu, D. Sun, S. Wang, Y.X. Hu, T.E. Lin, Z.F. Jia, L.Z. Wang, Polyethylenimine expanded graphite oxide enables high sulfur loading and long-term stability of lithium-sulfur batteries, Small 15 (2019) 1804578.

[40] Z.H. Shen, M.Q. Cao, Z.L. Zhang, J. Pu, C.L. Zhong, J.C. Li, H.X. Ma, F.J. Li, J. Zhu, F. Pan, H.G. Zhang, Efficient Ni2Co4P3 nanowires catalysts enhance ultrahigh-loading lithium-sulfur conversion in a microreactor-like battery, Adv. Funct. Mater. 30 (2020) 1906661.